

Recurrent computations for visual pattern completion

Hanlin Tang^{1,4*}, Bill Lotter^{1,3,4*}, Martin Schrimpf^{2,4*}, Ana Paredes⁴, Josue Ortega Caro⁴, Walter Hardesty⁴, David Cox³, Gabriel Kreiman⁴ [✉]

*These authors contributed equally

[✉]To whom correspondence should be addressed at

gabriel.kreiman@tch.harvard.edu

¹Program in Biophysics, Harvard University

²Program in Software Engineering, Augsburg University, Technische Universität München, Ludwig-Maximilians-Universität München

³Molecular and Cellular Biology, Harvard University

⁴Children's Hospital, Harvard Medical School

Text Statistics:

Number of words in abstract: 164

Number of words in significance statement: 100

Number of Figures: 4

Number of Tables: 0

Number of Supplementary Figures: 6

Abstract

Making inferences from partial information constitutes a critical aspect of cognition. During visual perception, pattern completion enables recognition of poorly visible or occluded objects. We combined psychophysics, physiology and computational models to test the hypothesis that pattern completion is implemented by recurrent computations and present three pieces of evidence that are consistent with this hypothesis. First, subjects robustly recognized objects even when rendered <10% visible, but recognition was largely impaired when processing was interrupted by backward masking. Second, invasive physiological responses along the human ventral cortex exhibited visually selective responses to partially visible objects that were delayed compared to whole objects, suggesting the need for additional computations. These physiological delays were correlated with the effects of backward masking. Third, state-of-the-art feed-forward computational architectures were not robust to partial visibility. However, recognition performance was recovered when the model was augmented with attractor-based recurrent connectivity. These results provide a strong argument of plausibility for the role of recurrent computations in making visual inferences from partial information.

Introduction

Humans and other animals demonstrate a remarkable ability to make inferences from partial data across all cognitive domains, ranging from interpreting sensory information to understanding social interactions. In the visual domain, this capacity is ubiquitously illustrated during pattern completion to recognize objects that are rendered partially visible due to noise, limited viewing angles, poor illumination or occlusion.

There has been significant progress in describing the neural machinery along the ventral visual stream responsible for recognizing whole objects (1-7).

Computational models instantiating biologically plausible algorithms for pattern recognition of whole objects typically consist of a sequence of linear filtering and non-linear pooling operations. The concatenation of these operations transforms the pixel inputs into a feature representation that is amenable for linear decoding of object labels. This family of feed-forward algorithms performs quite well in large scale computer vision experiments for pattern recognition (e.g., (8)) and also provides a first-order approximation to describe the activity of neurons along the ventral visual stream (e.g., (9)).

Despite the success of these feed-forward architectures in describing the initial steps in visual recognition, each layer has limited spatial integration of its inputs. Additionally, feed-forward algorithms generally lack mechanisms to integrate temporal information or to take advantage of the rich temporal dynamics characteristic of neural circuits that allow comparing signals within and across different levels of the visual hierarchy. Both spatial and temporal integration are likely to play an important role in pattern completion mechanisms (10-16). When an object is occluded, there are infinitely many possible contours that could join the object's parts together. Yet, the brain typically manages to integrate those parts to correctly recognize the occluded object. Multiple studies have highlighted the importance of temporal integration for pattern completion by demonstrating that recognizing partially visible objects takes more time than recognizing fully visible

ones, both at the behavioral level (11, 17), as well as at the physiological level (12, 14, 16).

We conjectured that recurrent computations, including potentially both within-layer horizontal connections as well as top-down signals along the ventral visual stream, are involved in implementing the spatial and temporal integrative mechanisms underlying pattern completion. Recurrent connections can link signals over space within a layer and provide specific top-down modulation from neurons with larger receptive fields (18, 19). Additionally, recurrent signals temporally lag their feed-forward counterparts and therefore provide an ideal way to incorporate neural dynamics and temporal integration mechanisms.

In order to examine plausible mechanisms involved in pattern completion, we combined psychophysical experiments, neurophysiological recordings (14), and computational modeling to evaluate recognition performance using a common set of objects rendered under poor visibility. We first show that humans are able to robustly recognize objects despite the limited amount of information available during the task, but performance rapidly deteriorates when computations are interrupted by the introduction of a noise mask. Furthermore, on an image-by-image basis, the behavioral effect of such backward masking correlates with an increase in latency in neurophysiological signals along the ventral visual stream. We then demonstrate that modern feed-forward computer vision models are not robust to occlusion and that the breakdown of their representation for individual images correlates at the image-by-image level with an increase in physiological latency. Finally, we extend previous notions of attractor dynamics by adding recurrence to a state-of-the-art model of visual recognition and provide a proof-of-concept model that captures the essence of human pattern completion behavior.

Results

Robust recognition of partially visible objects

Twenty-one subjects performed a visual recognition task (**Figure 1A-B**) involving categorization of objects that were either partially visible by presenting

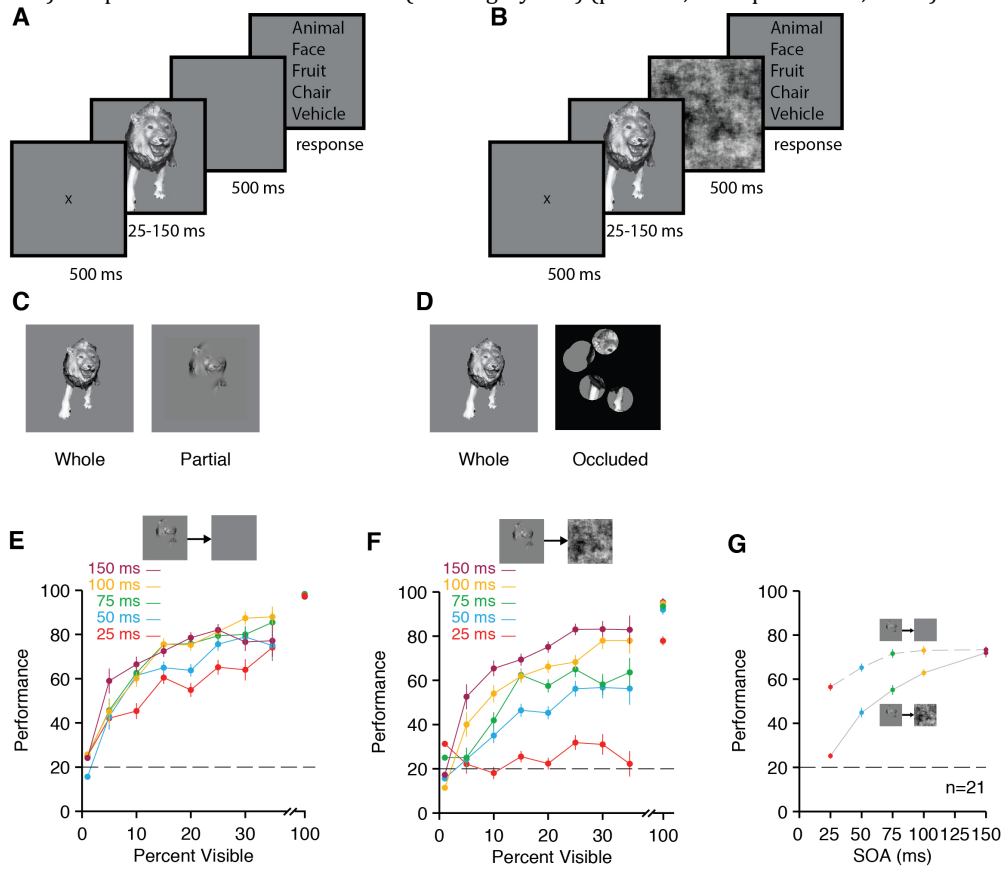
them through bubbles (“Partial”, **Figure 1C**) or fully visible (“Whole”, **Figure 1D**). The images were followed by either a gray screen (“unmasked”, **Figure 1A**) or a spatially-overlapping noise pattern (“masked”, **Figure 1B**) for 500 ms. The image presentation time, referred to as stimulus onset asynchrony (SOA), ranged from 33 to 150 ms in different trials presented in random order. In the main experiment, stimuli consisted of 325 objects belonging to five categories (animals, chairs, faces, fruits, vehicles). Each object was only presented once in each condition. The parts revealed for each object were chosen randomly. We considered a total of 40 images per object, comprising a total of 13,000 images of partial objects (**Methods**).

We start by describing the psychophysics results in the absence of a mask. For whole objects, behavioral performance was near ceiling, as expected (**Figure 1E**, 100% visible). Subjects were able to robustly recognize partial objects across a wide range of visibility levels despite the limited information provided (**Figure 1E**, note the cut in the x-axis). Although poor visibility degraded performance with respect to whole objects, subjects still showed $80 \pm 3\%$ performance at $35 \pm 2.5\%$ visibility (comparison between partial and whole objects: $p < 10^{-10}$, two-sided t-test). Even for images with $10 \pm 2.5\%$ visibility, performance was well above chance levels ($59 \pm 2\%$, $p < 10^{-10}$, two-sided t-test, chance = 20%). There was a small but significant improvement in performance at longer SOAs for partially visible objects (**Figure 1G** dashed lines, Pearson’s correlation coefficient, henceforth referred to as Pearson r , $= 0.56$, $p < 0.001$, permutation test).

In a separate experiment, we used an explicit occluder to generate images where objects appeared behind a uniform black surface (**Figure 1D**). Consistent with previous studies (e.g. (15, 20)), recognition was also robust when using heavily occluded images. The presence of an occluder improved recognition performance with respect to recognition of partial objects (compare **Figure S1A** versus **S1B**, $p < 10^{-4}$, Chi-squared test). In the following experiments, unless otherwise stated, we focused on the essential aspects of pattern completion by considering the more challenging condition of partially visible objects, without help from other cues such as occluders.

Figure 1. Backward masking disrupts recognition of partially visible objects

(A-B) Twenty-one subjects performed a forced-choice categorization task. After 500ms of fixation, stimuli were presented for variable exposure times (25 to 150 ms), denoted as the stimulus onset asynchrony (SOA). The image was followed either by a gray screen (**A**) or a noise mask (**B**) for 500 ms, after which the response choice screen was shown. **(C)** Stimuli were either presented unaltered ('Whole' condition) or rendered partially visible ('Partial' condition). **(D)** In a variant experiment, stimuli were occluded (results shown in **Figure S1**). **(E-F)** Behavioral performance as a function of the percentage of the object that was visible for the unmasked (**E**) and masked (**F**) trials. The colors denote different SOAs. Error bars denote s.e.m. ($n=21$ subjects). Horizontal dashed line indicates chance level (20%). Bin size = 2.5%. Note the discontinuity introduced in the x-axis to report performance for whole objects (single point at 100% visibility, SOA=150 ms). **(G)** Average recognition performance as a function of the stimulus onset asynchrony (SOA) for partial objects (same data and color scheme as **E-F** shown here as a function of SOA and excluding 100% visible point). Error bars denote s.e.m. Performance was significantly degraded by masking (solid gray line) compared to the unmasked trials (dotted gray line) ($p<0.001$, Chi-squared test, d.f.=4).



Backward masking disrupts recognition of partially visible objects

Multiple lines of evidence from behavioral (e.g. (21, 22)), physiological (e.g. (23-26)), and computational studies (e.g. (4, 5, 9, 27, 28)) suggest that recognition of whole isolated objects can be approximately described by rapid, largely feed-forward, mechanisms. Several investigators have used psychophysical experiments involving backward masking in an attempt to force the visual recognition machinery

to operate in a fast regime with minimal influences from recurrent signals (e.g. (29)): when an image is rapidly followed by a spatially overlapping mask, the new high-contrast mask stimulus interrupts any additional, presumably recurrent, processing of the original image (23, 30-38). We asked whether this fast, essentially feed-forward, recognition regime imposed by backward masking is sufficient for robust recognition of partially visible objects by randomly interleaving trials with a mask (**Figure 1B**).

The behavioral effects of backward masking are shown in **Figure 1F**. Performance for whole images was affected by the mask only for the shortest SOA values (cf. **Figure 1E** versus **1F** at 100% visibility, $p < 0.01$, two-sided t-test). When partial objects were followed by a backward mask, performance was significantly impaired (compare **Figure 1E** versus **1F**). A two-way ANOVA on performance with SOA and masking as factors revealed a significant interaction ($F(4) = 42.6$, $p < 10^{-8}$). The behavioral consequences of shortening SOA were significantly stronger in the presence of backward masking (compare solid versus dashed lines in **Figure 1G** after averaging across visibility levels). Additionally, backward masking disrupted performance across a wide range of visibility levels, as demonstrated in **Figure 1F-G**. The effects of backward masking were significant at $SOA \leq 100$ ms. Similar effects of backward masking were observed when using occluded objects (**Figure S1B**, $F = 56.3$, $p < 0.001$, two-way ANOVA). In sum, interrupting processing via backward masking led to a large reduction in the ability for pattern completion of partially visible images and occluded images, across a wide range of SOA values and visibility levels.

Images more susceptible to backward masking elicited longer neural delays along human ventral visual cortex

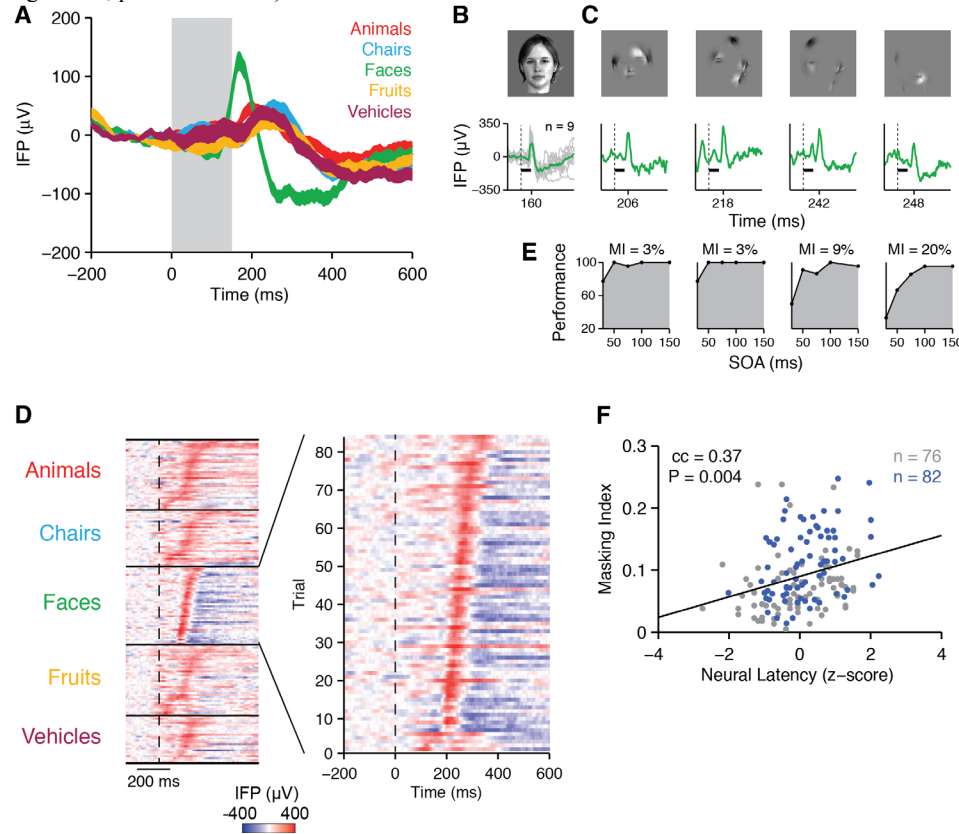
In a recent study, we recorded invasive physiological signals throughout the ventral visual stream in human patients with epilepsy while they performed an experiment similar to the one in **Figure 1A** (14). This experiment included 25 objects where images were presented for 150 ms without any masking. For whole objects, neural signals along the ventral visual stream showed rapid selective

responses to different object categories, as shown for an example electrode in the left fusiform gyrus in **Figure 2A-B**. When presenting partially visible objects, the neural signals remained visually selective (**Figure 2C-D**). The visually selective signals elicited by the partial objects were significantly delayed with respect to the responses to whole objects (compare the peak responses in **Figure 2C-D** with the peak response before 200 ms in **Figure 2A-B**). Because the visible features varied from trial to trial, different renderings of the same object elicited a wide distribution in the neural response latencies (**Figure 2C-D**). For example, the peak voltage occurred at 206 ms post stimulus onset in response to the first image on the right in **Figure 2C** and at 248 ms in response to the last image on the right in **Figure 2C**.

Heterogeneity across different renderings of the same object was also evident in the range of effects of backward masking at the behavioral level in the psychophysics experiment discussed in **Figure 1F-G**. We hypothesized that those images that elicited longer neural delays would also be more susceptible to backward masking. To test this hypothesis, we selected two of the recording sites in the neurophysiological study showing strong visually selective signals (one of these sites is shown in **Figure 2A-D**). We considered 650 images of partially visible objects corresponding to the 25 objects from the neurophysiology experiment. Using the same images (i.e. the exact same features revealed for each object), we conducted a separate psychophysics experiment to evaluate the effect of backward masking on each individual image (n=33 subjects). This experiment allowed us to construct a curve of behavioral performance as a function of SOA during backward masking, for each of the selected images from the neurophysiology experiment (**Figure 2E**). For example, the first image on the left in **Figure 2C** was less affected by backward masking than the last image on the right, particularly at short SOA values. To quantify the effect of backward masking, we defined a masking index, MI = 1-AUC, where AUC is the normalized area under the curve in the performance versus SOA plot (gray area in **Figure 2E**). Larger MI values correspond to larger effects of backward masking: MI ranges from 0 (no effect of backward masking) to 0.8 (backward masking leads to chance performance). The MI values were 3% and 20% for the first and last images in **Figure 2C** respectively.

Figure 2. The behavioral effect of masking correlated with the neural response latency on an image-by-image basis

(A) Invasive recordings of neural activity from the human brain while a subject was performing the task described in **Figure 1** (no masking, 150 ms presentation time). For an electrode in the left Fusiform gyrus, here we show the intracranial field potential (IFP) response averaged across five categories of whole objects. This electrode responded selectivity to faces (green line) compared to other categories. The gray rectangle indicates the stimulus presentation time (150 ms). The shaded area around each curve indicates s.e.m. For more detail about this electrode, see Fig. 2 in (14). (B) IFP responses for one of the whole objects for the same electrode in (A) showing single trial responses (gray, n=9) and average response (green). The latency of the peak response is marked on the x-axis. (C) Single-trial responses (n = 1) to 4 partial objects of the same object. (D) A new stimulus set for psychophysics experiments was constructed from the images in 650 trials from two electrodes in the physiology experiments. For the example electrode in A, this subplot shows a raster of the neural responses, one trial per line, from partial trials that were selected for psychophysics testing. These trials elicited strong physiological responses with a wide distribution of response latencies. The color indicates the voltage (see color scale on bottom). The inset (right) zooms in on the responses to the n=82 trials in the preferred category. (E) We conducted a separate psychophysics experiment to measure the effect of backward masking at various SOAs for each of the same partial exemplar images used in the physiology experiment (n=33 subjects). We computed a masking index (MI) for each image defined as 1 - the area under the curve in the performance versus SOA plots (**Methods**). The larger the MI for a given image, the stronger the effect of masking. (F) Correlation between the effect of backward masking (y-axis, MI as defined in E) and the neural response latency (x-axis, as defined in B-C). Each dot is a single partial object from the preferred category for electrode 1 (blue) or 2 (gray). There was a significant correlation (Pearson $r = 0.37$, $P = 0.004$, linear regression, permutation test).



For those images from the preferred category for each electrode, the masking index showed a weak but significant correlation with the neural response latency, even after accounting for image difficulty and recording site differences (**Figure 2F**,

Pearson $r = 0.37$, $p = 0.004$, permutation test, **Methods**). This effect was stimulus selective: the masking index was *not* correlated with the neural response latency for images from the non-preferred categories ($p = 0.33$, permutation test). Although the physiology and behavioral experiments were conducted in different subjects, we found that images that led to longer neural response latencies were associated with a stronger effect of interrupting computations via backward masking.

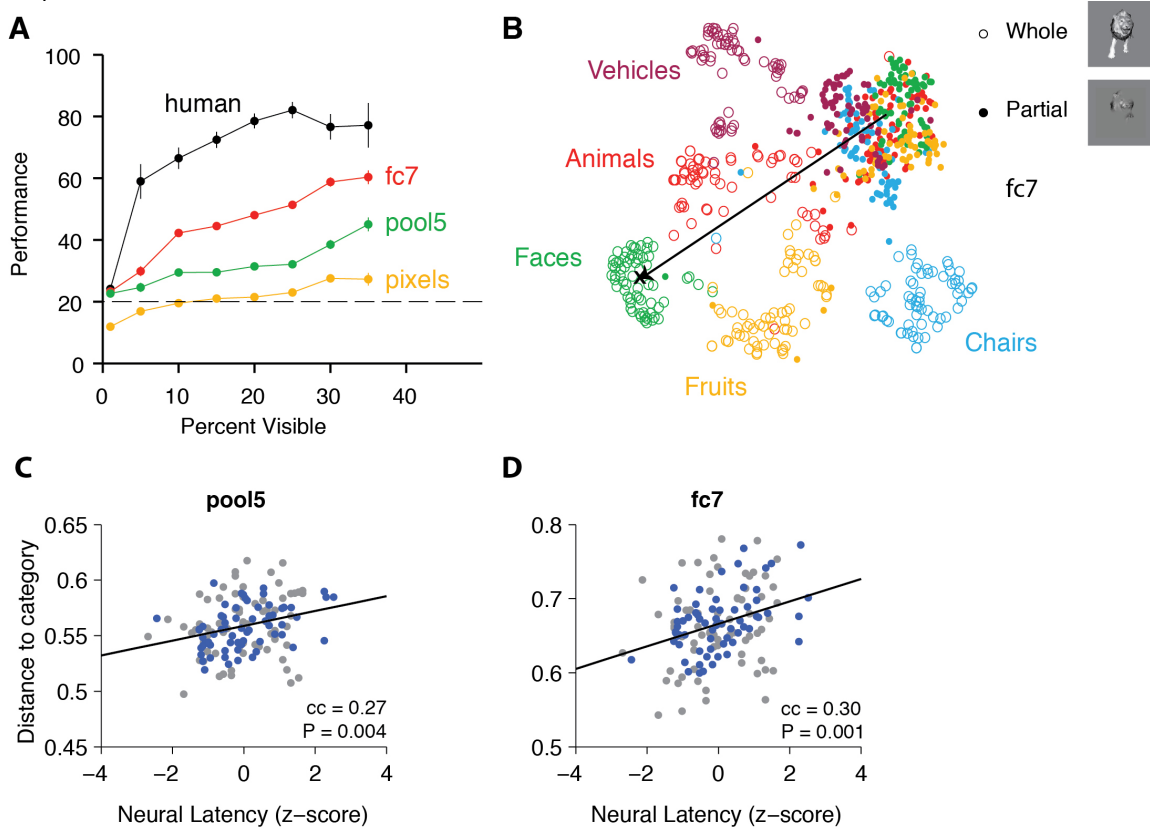
Standard feed-forward models are not robust to occlusion

We next set out to investigate the potential computational mechanisms involved in pattern completion responsible for the behavioral and physiological observations described in **Figures 1-2**. We began by considering state-of-the-art implementations of the family of purely feed-forward computational models of visual recognition. These computational models are characterized by hierarchical, feed-forward processing with progressive increases in the size of receptive fields, the degree of selectivity, and tolerance to object transformations (e.g. (4, 5, 27, 39)). Such models have been successfully used to describe rapid recognition of whole objects at the behavioral level (e.g. (5)) as well as neuronal firing rates in areas V4 and inferior temporal cortex in the macaque monkey (e.g. (9)). Additionally, these deep convolutional network architectures achieve high performance in computer vision competitions evaluating object recognition capabilities (e.g. (8, 40)).

We evaluated whether these feed-forward models could lead to successful recognition of partially visible objects using the same set of 325 objects (13,000 trials) in **Figure 1**. As a representative of this family of models, we considered AlexNet, an eight-layer convolutional neural network trained via back propagation (41) on ImageNet, a large corpus of natural images (8). We used as features either activity in the last fully connected layer before readout (fc7, 4096 units), or activity in the last retinotopic layer (pool5, 9216 units). In order to measure the effect of low-level differences between categories (contrast, object area, etc.), we also considered raw pixels as baseline performance ($256^2 = 65,636$ features).

Figure 3: Standard feed-forward models were not robust to occlusion

(A) Performance of various feed-forward computational models (colors) compared to human performance (black). For each model, we used its feature representation, trained an SVM classifier on whole objects, and evaluated its performance on the feature representation of partial objects (**Methods**). The objects used to train the classifier did not appear as partial objects in the test set. Human performance is shown here (150 ms SOA) from the same set of images (black). Error bars denote s.e.m. (5-fold cross-validation). (B) We applied dimensionality reduction using stochastic neighborhood embedding (t-SNE, **Methods**) to visualize the fc7 representation in the AlexNet model. Both whole objects (open circles) and partial objects (closed circles) from different categories are separable in this space, but the boundaries learned on whole objects did not generalize to the space of partial objects. The black arrow shows a schematic example of model distance definition, from an image of a partial face (green circle) to the average face centroid (black cross). (C-D) The neural latency for each image was correlated with the distance of the image to the category center for the models. Correlation between the distance from each partial object to its whole category center (schematically illustrated in **Figure 3B**) and the neural response latency (defined in **Figure 2B**). Each dot represents a partial object with responses recorded either from electrode 1 (blue dots) or electrode 2 (gray dots). Results are shown for two models (C: AlexNet-pool5, D: AlexNet-fc7). The correlation coefficients and p values from the permutation test are shown for each subplot.



We sought to measure the robustness of these networks to partial object visibility in the same way that other studies have evaluated tolerance to other transformations such as size and position changes, i.e., by training a decision boundary on one condition and testing on the other conditions (e.g. (5, 24)). We thus trained the decision boundaries using a support vector machine classifier with a linear kernel on the representation of the 325 whole objects of the stimulus set from **Figure 1**, and then tested object categorization performance on images of

partial objects. Cross-validation was performed over objects: objects used to train the decision boundary did not appear as partial objects in the test set. The performance of raw pixels was essentially at chance level (**Figure 3A**). In contrast, the other models performed well above chance ($p < 10^{-10}$, two-sided t-test). The AlexNet fc7 layer demonstrated better performance than the pool 5 layer. While these feed-forward models performed well above chance, there was a significant gap with respect to human performance, at all visibility levels below 40% ($p < 0.001$, Chi-squared test, **Figure 3A**). These results are consistent with those reported in other experimental simulations with occluded objects and similar bottom-up neural networks (42). The observation that bottom-up models perform below humans in recognition of partially visible images depends strongly on the stimuli and on the amount of information available: bottom-up models were comparable to humans when visibility was above 50% (**Figure S2**, (43)).

To visualize the effect of partial visibility on the model representations, we used stochastic neighborhood embedding (t-SNE (44)), a dimensionality reduction technique, that projects the features from the fc7 layer of AlexNet onto two dimensions (**Figure 3B**). As expected, the representation of whole objects (open circles) showed a clear separation among categories. However, partial objects from different categories (filled circles) were more similar to each other than to whole objects from their corresponding categories. Therefore, decision boundaries trained on whole objects did not generalize to categorization of partial objects, as demonstrated in **Figure 3A**. These results are consistent with a previous computational study, using feed-forward models similar to the ones in the current work and evaluating a more extensive image data set (42). Thus, despite the success of purely feed-forward models in recognition of whole objects, these models were not robust to images with severely reduced amounts of visibility and did not account for human performance levels in pattern completion for low visibility objects.

We next sought to further understand the breakdown in the models' representations of objects under partial visibility. As illustrated by the t-SNE plot, removing large amounts of pixels from the objects pushed the model's

representation of the partially visible images a large distance away from their whole counterparts (see for example the arrow in **Figure 3B**). The distance between the representation of a partially visible object and the corresponding whole object category mean is indicative of the magnitude of the impact of partial visibility on the object representation. We evaluated whether the distortion in the feed-forward representation caused by partial visibility was correlated with the latencies in the neural recordings discussed in **Figure 2**. We reasoned that images of partial objects whose model representation was more distorted would lead to longer neural response latencies. We computed the Euclidean distance between the representation of each partial object and the category mean in the representation of whole objects for the pool5 and fc7 computational models. This distance is *schematically* illustrated for one image and the fc7 model by the black arrow in **Figure 3B**, but we note that the actual distances were computed using all the fc7 features and not using the graphical t-SNE representation. We found a modest but significant correlation at the object-by-object level between the computational distance to the category mean and the neural response latency for the pool5 (**Figure 3C**) and fc7 (**Figure 3D**) features. The statistical significance of these correlations was assessed by regressing the distance to category mean against the neural latency, along with several additional predictors to account for potential confounds. Specifically, we included the following factors: (i) the percentage of object visibility and pixel distance to regress out any variation explained by low-level effects of occlusion as well as difficulty; (ii) the electrode number to account for the inter-electrode variability in our dataset, and (iii) the masking index (**Figure 2E**), to control for overall recognition difficulty. The model distance to category mean in the pool5 and fc7 layers correlated with the response latency beyond what could be explained by these additional factors (pool 5: Pearson $r = 0.27, p=0.004$, permutation test; fc7: Pearson $r = 0.3, p=0.001$, permutation test). In sum, state-of-the-art feed-forward architectures did not robustly extrapolate from whole to partially visible objects and failed to reach human-level performance in recognition of partially visible objects. The representation of partially visible objects was sufficiently distinct from that of whole objects, leading to misclassification. As the

difference in the representation of whole and partial objects increased, the time it took for a selective neural response to evolve in response to the partial object was also longer.

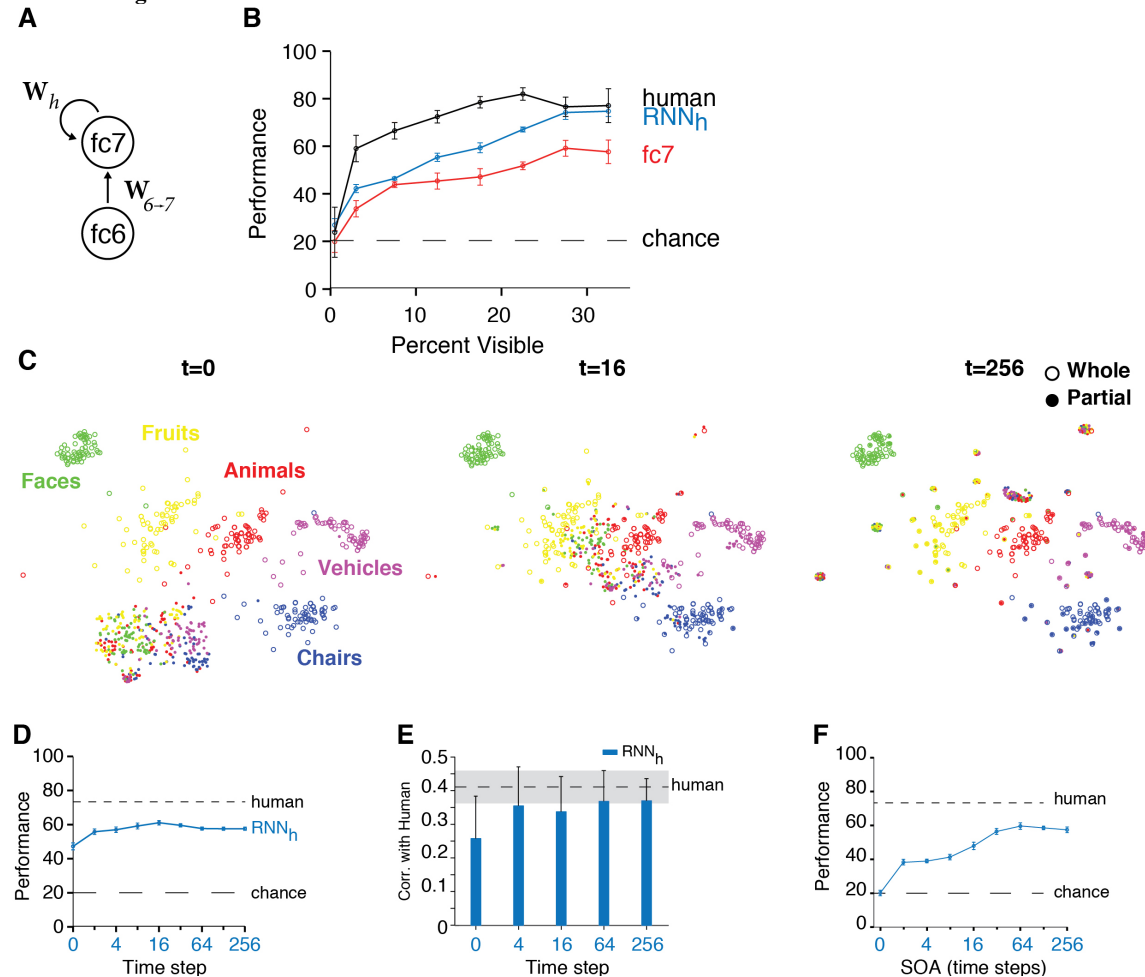
Recurrent neural networks improve recognition of partially visible objects

The behavioral, neural and modeling results presented above suggest a need for additional computational steps beyond those present in feed-forward architectures to build a robust representation for partially visible objects. Several computational ideas, originating from models proposed by Hopfield (45) have shown that attractor networks can perform pattern completion. In the Hopfield network, units are connected in an all-to-all fashion with weights defining fixed attractor points dictated by the whole objects to be represented. In this framework, images that are pushed farther away by limited visibility would require more processing time to converge to the appropriate attractor, consistent with the behavioral and physiological observations. As a proof-of-principle, we augmented the feed-forward models discussed in the previous section with recurrent connections in an attempt to generate a robust representation through an attractor-like mechanism for each whole object (**Figure 4A**). Specifically, we used the AlexNet architecture with fixed feed-forward weights from pre-training on ImageNet (as in **Figure 3**) and added recurrent connections to the fc7 layer. Recurrent connectivity is ubiquitous throughout *all* visual neocortical areas in biological systems. The motivation to include recurrent connectivity *only* in the fc7 layer was to examine first a simple and minimal extension to the existing architectures (Discussion).

We denote the activity of the fc7 layer at time t as the 4096-dimensional feature vector \mathbf{h}_t . At each time step, the activity \mathbf{h}_t was determined by a combination of the activity from the previous time step \mathbf{h}_{t-1} and the constant input drive from the previous layer \mathbf{x} : $\mathbf{h}_t = f(\mathbf{W}_h \mathbf{h}_{t-1}, \mathbf{x})$ where f introduces a non-linearity (see **Methods** for further details). The input from the previous layer, fc6, was kept constant over time, and is identical to the fc6 input in the purely feed-forward AlexNet architecture. \mathbf{W}_h is a weight matrix that governs the temporal evolution of the fc7 layer.

Figure 4: A dynamic recurrent neural network showed improved performance over time, and was impaired by backward masking

(A) The top-level representation in AlexNet (fc7) receives inputs from fc6, governed by weights $W_{6 \rightarrow 7}$. We added a recurrent loop within the top-level representation (RNN). The weight matrix W_h governs the temporal evolution of the fc7 representation. The different ways of choosing the set of weights W_h led to two types of recurrent models: RNN_h (Hopfield) shown here, and $RNN_{1,5}$ trained on partial objects (with RNN_1 trained on only one category and RNN_5 trained on all 5 categories) discussed in the text and shown in **Figures S4-S5**. (B) Performance of the recurrent neural networks RNN_h (blue) as a function of object visibility. RNN_h approached human performance (black curve), and represented a significant improvement over the original fc7 layer (red curve). Dashed line indicates chance. The red and black curves are the same ones depicted in **Figure 3A** and are reproduced here for comparison purposes. Error bars denote SEM. (C) Temporal evolution of the feature representation for RNN_h as visualized with t-SNE (format as in **Figure 3B**). Whole objects (open circles) and partial objects (closed circles) are colored according to their category. For visualization purposes, only one partial object of each object is shown. Over time, the representation of partial objects approaches the correct category in the clusters of whole images. (D) Overall performance of RNN_h as a function of recurrent time step compared to human performance (top dashed line) and chance (bottom dashed line). Error bars denote s.e.m. (5-way cross-validation, Methods). (E) Correlation in the pattern of responses between the recurrent model and humans. Dashed line indicates the upper bound of human-human similarity obtained by computing how well half of the subject pool correlates with the other half. Regressions were computed separately for each category -- to avoid the differences across categories to dominate the correlations -- followed by averaging the correlation coefficients across categories. Over time, the model becomes more human-like. Error bars denote S.D. across categories. (F) Effect of backward masking. The same backward mask used in the psychophysics experiments was fed to the RNN_h model at different SOA values (x-axis) and performance was evaluated at multiple time steps. Error bars denote s.e.m. (5-way cross-validation). Performance improved with increasing SOA values as demonstrated for humans in **Figure 1G**.



We considered a Hopfield network, RNN_h , without introducing any free

parameters that depended on the partial objects, where \mathbf{W}_h was a symmetric weight matrix dictated by the fc7 representation of the whole objects (**Methods**). The initial state of the network was given by the activity in the previous layer, $\mathbf{h}_0 = \mathbf{W}_{6 \rightarrow 7} fc6$, followed by binarization. The state of the network evolved over time according to $\mathbf{h}_t = satlins(\mathbf{W}_h \mathbf{h}_{t-1})$ for $t > 0$ where *satlins* is a saturating non-linearity (**Methods**). We first verified that each one of the whole objects constituted an attractor point in the network by ensuring that their representation did not change over time when used as inputs to the model. We next evaluated the responses of RNN_h to all the images containing partial objects. The model was run until convergence (i.e. until none of the signs of any of the features changed between consecutive time steps). Based on the final time point, we evaluated the performance of this model in recognizing partially visible objects. The RNN_h demonstrated a significant improvement over the AlexNet fc7 layer (**Figure 4B**, $57 \pm 0.4\%$, $p < 0.001$, Chi-squared test).

The dynamic trajectory of the representation of whole and partial objects in the fc7 layer of the RNN_h model is visualized in **Figure 4C**. Before any recurrent computations have taken place, at $t=0$ (left), the representations of partial objects were clustered together (closed circles) and separated from the clusters of whole objects in each category (open circles), as described in **Figure 3B**. As time progressed, the cluster of partial objects was pulled apart and moved towards their respective categories. For example, at $t=16$ (center) and $t=256$ (right), the representation of partial chairs (closed blue circles) largely overlapped with the cluster of whole chairs (open blue circles). Concomitant with this dynamic transformation in the representation of partial objects, the overall performance of the RNN_h model improved over time (**Figure 4D**).

In addition to the average performance reported in **Figure 4B** and **4D**, we directly compared performance at the object-by-object level between humans and RNN_h (**Figure S3A**). Over time, RNN_h behaved more like humans at the object-by-object level (**Figure 4E**). For each time step in the model, we computed the average correct rate on partial objects for each object, from each of the 5 categories, and

correlated this vector with the pattern of human performance (see **Figure S3A** for the correlation plots). The upper bound (dashed line in **Figure 4E**) represents human-human similarity, defined as the correlation in the response patterns between half of the subject pool and the other half. Over time, the recurrent model-human correlation increased towards the human-human upper bound. We also examined the correlations across all of the objects irrespective of their category; these correlations also improved over time but were dominated by the across-category differences in performance.

In sum, implementing recurrent connections in an attractor-like fashion at the top of a feed-forward hierarchical model significantly improved the model's performance in pattern completion, and the additional computations were consistent with temporal delays described at the behavioral and neural levels.

Backward masking impaired RNN model performance

We reasoned that the backward mask introduced in the experiment discussed in **Figure 1B, F, G** impaired recognition performance by interrupting processing and we set out to investigate whether we could reproduce this effect in the RNN_h model. We computed the responses of the AlexNet model to the mask and fed these fc6 features for the mask to the RNN_h model after a certain number of time steps. Switching the mask input on at earlier time points was meant to mimic shorter SOA's in the psychophysical experiments. We read out performance based on the resulting activity combining the partial object and the mask at different time points (**Figure 4F**). Presenting the mask reduced performance from 58±2% (SOA=256 time steps) to 37±2% (SOA=2 time steps). Although we cannot directly compare SOAs expressed in milliseconds in the behavioral experiments to time steps in the model, these results are qualitatively consistent with the behavioral effects of backward masking (**Figure 1G**),

Discussion

Under natural viewing conditions, it is routinely necessary to recognize objects that are partially visible due to occlusion and poor illumination. The visual

system is capable of completing patterns and making inferences under such conditions even when only 10-20% of the object is visible (**Figure 1E**). Here we investigated the mechanisms underlying such robust recognition of partially visible objects at the behavioral, physiological and computational levels. We demonstrated that backward masking significantly impairs recognition of partial images at short stimulus onset asynchrony ($25\text{ms} \leq \text{SOA} \leq 100\text{ ms}$) (**Figures 1F-G**). The strength of the disruptive effect of backward masking on an image-by-image basis was correlated with the neural delays described previously (14) from invasive recordings along the ventral visual stream (**Figure 2**). A state-of-the-art bottom-up computational architecture trained on whole objects failed to achieve robustness in recognition of partially visible objects (**Figure 3A**). The introduction of recurrent connections to the top layer of this computational model led to significant improvement in recognition of objects from partial information both at the average level (**Figure 4B**) and at the object-by-object level (**Figure 4E**). The increase in performance involved recurrent computations evolving over time that were interrupted by the introduction of a mask (**Figure 4F**).

In most of the experiments in this study, we rendered objects partially visible by presenting them through “bubbles” (**Figure 1B**) in an attempt to distill the basic mechanisms required for spatial integration during pattern completion. Quantitatively, it is easier to recognize objects behind a real occluder (**Figure S1**, see also the classic demonstration in (20)). The results presented here were qualitatively similar (**Figure S1**) when using explicit occluders (**Figure 1D**): recognition of objects shown through explicit occluders is also disrupted by backward masking (**Figure S1**).

Recognition of partially visible objects requires longer reaction times (11, 17). Additionally, neural signals involved in representing partially visible objects show significant delays with respect to the corresponding responses representing continuous lines and whole objects (12, 14, 16). These behavioral and neural delays suggest the need for additional computational steps to interpret partially visible images. This notion is further supported by the observation that interrupting those additional computations by introducing a backward mask significantly impairs

recognition (**Figure 1F, G**). Several lines of evidence suggest that backward masking disproportionately affects recurrent computations (23, 30-38). Accordingly, we conjectured that the disruptive effect of backward masking during pattern completion could be ascribed to the impairment of such recurrent computations. Several investigators have argued that the rapid and selective signals along the ventral visual stream, which enable recognition of whole objects within approximately 100 ms of stimulus onset, reflect largely bottom-up processing (e.g. (4, 5, 9, 21-28) among many others). The long physiological delays of about 50 ms during recognition of partial objects (12, 14) provide ample time for recurrent connections to exert their effects during pattern completion. Indeed, several physiological studies have shown that recurrent signals are accompanied by delays of approximately 50 ms throughout ventral visual cortex (e.g. (18, 46, 47)). These delays of approximately 50 ms duration could be accounted for by the recruitment of lateral/horizontal recurrent connections within a visual area or top-down signals from higher visual areas. The current results do not allow us to disambiguate horizontal and top-down effects and both could contribute to pattern completion.

A related interpretation of the current findings is that more challenging tasks, such as recognizing objects from minimal pixel information, may lead to “slower processing” throughout the ventral visual stream. According to this idea, each neuron would receive weaker inputs and require a longer time for integration, leading to the longer latencies observed experimentally at the behavioral and physiological level. It seems unlikely that the current observations could be fully accounted by longer integration times at all levels of the visual hierarchy. First, all images were contrast normalized to avoid any overall intensity effects. Second, neural delays for poor visibility images were not observed in early visual areas (14). Third, the correlations between the effects of backward masking and neural delays persisted even after accounting for difficulty level (**Figure 3**). Fourth, none of the state-of-the-art purely bottom-up computational models were able to account for human level performance (see further elaboration of this point below). These arguments rule out slower processing throughout the entire visual system due to low intensity signals in the lower visibility conditions. However, the results

presented here are still compatible with the notion that the inputs to higher-level neurons in the case of partial objects could be weaker and could require further temporal integration. This possibility is consistent with the model proposed here. Because the effects of recurrent computations are delayed with respect to the bottom-up inputs, we expect that any such slow integration would have to interact with the outputs of recurrent signals.

In order to model and quantify the notion that recurrent connections could facilitate pattern completion, we presented a proof-of-principle model that extended bottom-up architectures by adding recurrent connections at the top level (**Figure 4A**). This simple extension significantly improved performance (**Figure 4B**), showed a correlation at the object-by-object level (**Figure 4E**) and also qualitatively accounted for the effects of backward masking (**Figure 4F**). The RNN_h model had no free parameters that depended on the partial objects and all the weights were fully determined by the features representing whole objects in the last layer.

A potential challenge with this type of architecture is the pervasive presence of spurious attractor states, particularly prominent when the network is near capacity. Furthermore, this simple instantiation of a recurrent architecture still performs below humans, particularly under very low visibility conditions. It is conceivable that more complex architectures that take into account the known lateral connections in every layer as well as top-down connections in visual cortex might improve performance even further.

One way of increasing the complexity and power of the model is to directly train the network with partially visible objects. We extended the recurrent computations in the Hopfield model to a family of RNN models where the W_h weights were directly trained to minimize, over time, the distance in the fc7 layer between the partial object and the corresponding whole object (**Methods**). Importantly, to avoid overfitting, we used a subset of the objects for training W_h , and then tested the model's classification performance on a new set of objects. This model, which we denote as RNN_5 , had 4096^2 recurrent weights trained on a subset of the objects from all five categories. The RNN_5 model significantly outperformed the fc7 and RNN_h models (**Figure S4**). Considering all levels of visibility, the RNN_5

model performed slightly above human levels ($p=3 \times 10^{-4}$, Chi-squared test). While the RNN₅ model can extrapolate across objects and categorize images of partial objects that it has not seen before, it does so by exploiting features that are similar for different objects within the 5 categories in the experiment. RNN₁, a model where the recurrent weights were trained using solely objects from one of the categories and performance was evaluated using objects from the remaining 4 categories, did not perform any better than the purely feed-forward architecture (**Figure S5**, $p=0.05$, Chi-squared test). Upon inspection of the fc7 representation, we observed that several of the features were sparsely represented across categories. Therefore, the recurrent weights in RNN₁ only modified a fraction of all the possible features, missing many important features to distinguish the other objects. Thus, the improvement in RNN₅ is built upon a sufficiently rich dictionary of features that are shared among objects within a category. These results show that recurrent neural networks trained with subsets of the partially visible objects can achieve human level performance, extrapolating across objects, as long as they are trained with a sufficiently rich set of features. A fundamental distinction between RNN_h and RNN₅ is that the latter model requires training with partial objects. It is unclear whether humans require specific experience with partial objects to perform pattern completion. Although the specific photographs of objects used in the psychophysics experiments presented here were new to the subjects, humans have extensive experience in recognizing objects from partial information. Extrapolating from the simplified models presented here, it may be inferred that humans might be able to recognize novel objects that are partially visible based on experience with their whole counterparts exclusively, but may need direct experience with the partial objects in cases of extremely low visibility.

Before examining these recurrent models, we analyzed bottom-up architectures and showed that they were *not* robust to extrapolating from whole objects to partial objects (**Figure 4**). However, there exist infinitely many possible bottom-up models. Hence, even though we examined state-of-the-art models that are quite successful in object recognition, the failure to account for the behavioral and physiological results in the bottom-up models examined here (as well as similar

failures reported in other studies, e.g. (42)) should be interpreted with caution. We do not imply that it is impossible for *any* bottom-up architecture to recognize partially visible objects. In fact, it is possible to unfold a recurrent network with a finite number of time steps into a bottom-up model by creating an additional layer for each additional time step. However, there are several advantages to performing those computations with a recurrent architecture including a drastic reduction in the number of units required as well as in the number of weights that need to be trained and the fact that such unfolding is applicable only when we know *a priori* the fixed number of computational steps required, in contrast with recurrent architectures that allow an arbitrary and variable number of computations.

While it is unclear how to directly map the time steps in each recurrent computation to real time in milliseconds, all of the RNN versions involve a dynamic evolution of the representation of features in partial objects (**Figure 4C-F**). These dynamic changes bring the representation of partial objects closer to that of whole objects. As a first approximation, these computational dynamics, map onto the temporal lags observed at the behavioral and physiological levels. Furthermore, these dynamics are interrupted by the presentation of a backward mask in close temporal proximity to the image (**Figure 1F-G, 4F**).

Under natural viewing conditions, there are multiple other cues that can aid recognition of partially visible objects including understanding of textures, relative positions, segmentation, movement, source of illumination, and stereopsis, among others. None of these mechanisms were considered in the current instantiation of the models. It will be interesting to integrate these additional sources of information to understand how they contribute to the mechanisms of pattern completion under real world conditions. The convergence of behavioral, physiological and theoretical evidence presented here provides an initial path and a biologically constrained hypothesis to understand the role of recurrent computations during pattern completion.

Methods

Psychophysics experiments

A total of 83 volunteers (32 male, ages 18-31) with normal or corrected to normal vision participated in the psychophysics experiments reported in this study. All subjects gave informed consent and the studies were approved by the Institutional Review Board. In 46 subjects, eye positions were recorded using an infrared camera eye tracker at 500 Hz (SR Research, Ontario, Canada). We performed a main experiment (reported in **Figure 1**) and two variations (reported in **Figure 2** and **Figure S1**).

Main experiment. A scheme of the experiment is shown in **Figure 1**. Twenty-one subjects were asked to categorize images into one of 5 possible semantic groups (5-alternative forced choice) by pressing buttons on a gamepad. Stimuli consisted of contrast-normalized gray scale images of 325 objects belonging to five categories (animals, chairs, human faces, fruits, and vehicles). Each trial was initiated by fixating on a cross for at least 500 ms. After fixation, subjects were presented with the image of an object for a variable time (25 ms, 50 ms, 75 ms, 100 ms, or 150 ms), referred to as the stimulus onset asynchrony (SOA). The image was followed by either a noise mask (**Figure 1B**) or a gray screen (**Figure 1A**), with a duration of 500 ms, after which a choice screen appeared requiring the subject to respond. The noise mask was generated by scrambling the phase of the images, while retaining the spectral coefficients. The images (256 x 256 pixels) subtended approximately 5 degrees of the visual field. In approximately 15% of the trials, the objects were presented in unaltered fashion (the 'Whole' condition, **Figure 1C** left). In the other 85%, the objects were rendered partially visible by presenting visual features through Gaussian bubbles (48) (the 'Partial condition', standard deviation = 14 pixels, **Figure 1C** right). Each subject performed an initial training session to familiarize themselves with the task and the stimuli. They were presented with 40 trials of whole objects, then 80 calibration trials of occluded objects. During the calibration trials, the number of bubbles was titrated using a staircase procedure to achieve a task difficulty of 80% correct rate. The number of bubbles (but not their positions) was then kept constant for the rest of the experiment. Results from the

familiarization and calibration phase were not included in the analyses. Despite calibrating the number of bubbles, there was a wide range of degrees of occlusion because the positions of the bubbles were randomized. Each image was only presented once in the masked condition and once in the unmasked condition.

Variant experiment. In the variant experiment ($n = 33$ subjects), stimuli consisted of 650 images from five categories from which we had previously recorded neural responses (see below). The difference with the Main experiment is that here we used the exact same images that were used in the physiological recordings in order to directly compare the behavioral results and the physiological results for the same images (but not the same subjects).

Occlusion experiment. In the occlusion experiment (**Figure S1**, $n=14$ subjects in the partial objects experiment and $n =15$ subjects in the occlusion experiment), we generated occluded images that revealed the same sets of features as the partial objects, but contained an explicit occlude (**Figure 1D**) to activate amodal completion cues. The stimulus set consisted of 16 objects from 4 different categories. For comparison, we also collected performance with partial objects from this reduced stimulus set.

Neurophysiology experiments

The neurophysiological data analyzed in **Figures 3-4** were taken from the study reported in reference (14), to which we refer for further details. Briefly, subjects were patients with pharmacologically intractable epilepsy who had intracranial electrodes implanted for clinical purposes. All studies were approved by the hospital's Institutional Review Board and were carried out with the subjects' informed consent. Images of partial or whole objects were presented for 150 ms, followed by a gray screen for 650 ms. Subjects performed a five-alternative forced choice categorization task as described in **Figure 1**.

To construct the stimulus set for the variant experiment (**Figure 2**), we chose two electrodes that were visually selective for partial objects from this

neurophysiology data set, and identified the images presented in $n = 650$ trials for psychophysical testing. For the preferred category, only trials where the amplitude of the elicited neural response was in the top 50th percentile were included, and trials were chosen to represent a distribution of neural response latencies. After constructing this stimulus set, we performed psychophysical experiments with $n = 33$ subjects (Variant experiment) to evaluate the effect of backward masking for the exact same images for which we had physiological data. We had to select a subset of electrodes because the random bubble positions changed across experiments and it was not practical to conduct a separate psychophysics experiment for each of the electrodes in the original experiment. The electrode selection procedure was strictly dictated by the above-described physiological criteria and was performed before even beginning the psychophysics experiment. Here we focused on the neural latency, defined as the time of the peak in the physiological response, as shown in **Figure 2B**. A more extensive analysis of the physiological data was presented in (14).

Behavioral and neural data analysis

Masking Index. To quantify the effect of backward masking, we defined the masking index as 100%-pAUC, where pAUC is the percent area under the curve when plotting performance as a function of SOA (e.g. **Figure 2E**).

Correlation between masking index and neural latency. To determine the correlation between masking index and neural response latency, we combined data from the two recording sites by first standardizing the latency measurements (z-score, **Figure 2F**). We then used a linear regression on neural response latency with masking index, percent visibility, and recording site as predictor factors to avoid any correlations dictated by task difficulty or differences between recording sites. We used only trials from the preferred category for each recording site and reported the correlation and statistical significance in **Figure 2F**. As described in the text, there was no significant correlation between the masking index and neural latency when considering trials from the non-preferred category.

Correlation between model distance and neural response latency. As described below, we simulated the activity of units in several computational models in response to the same images used in the psychophysics and physiology experiments. To correlate the model responses with neural response latency, we computed the Euclidean distance between the model representation of partial and whole objects. We computed the distance between each partial object in the variant stimulus set and either its whole counterpart (distance-to-exemplar), or to the centroid of the whole images from the same category (distance-to-category). We then assessed significance by using a linear regression on the model distance versus neural response latency while controlling for masking index, percent visibility, and recording site as factors.

Feed-forward Models

We considered the ability to recognize partially visible images by state-of-the-art feed-forward computational models of vision (**Figure 3A**). First, we evaluated whether it was possible to perform recognition purely based on pixel intensities. Next, we evaluated the performance of the AlexNet model (8). AlexNet is an eight-layer deep convolutional neural network consisting of convolutional, max-pooling and fully-connected layers with a large number of weights trained in a supervised fashion for object recognition on ImageNet, a large collection of labeled images from the web (8). We used a version of AlexNet trained using *caffe* (49), a popular deep learning library. Two layers within the AlexNet were tested: pool5 and fc7. Pool5 is the last convolutional (retinotopic) layer in the architecture. fc7 is the last layer before the classification step and is fully connected, that is, every unit in fc7 is connected to every unit in the previous layer. The number of dimensions used to represent each object was $256^2=65536$ for pixels, 9216 for pool5 and 4096 for fc7.

Classification performance for each model was evaluated on a stimulus set consisting of 13,000 images of partial objects (generated from 325 objects from 5 categories). These were the same partial objects used to collect human performance

in the main experiment (**Figure 1**). We used a support vector machine (SVM) with a linear kernel to perform classification. We used 5-fold cross-validation across the 325 objects. Each split contained 260 objects for training, and 65 objects split for validation and testing, such that each object was used exactly in one validation and testing split, and such that there was an equal number of objects from each category in each split. Decision boundaries were fit on the training set using the SVM with the C parameter determined through the validation set by considering the following possible C values: $10^{-4}, 10^{-3}, \dots, 10^3, 10^4$. The SVM boundaries were fit using images of whole objects and tested on images of partial objects. Final performance numbers for partial objects were calculated on the full data set of 13,000 images -- that is, for each split, classification performance was evaluated on the partial objects corresponding to the objects in the test set, such that, over all splits, each partial object was evaluated exactly once.

To graphically display the representation of the images based on all 4096 units in the fc7 layer of the model in a 2D plot (**Figure 3B** and **4C**), we used stochastic neighborhood embedding (t-SNE) (44). We note that this was done exclusively for display purposes and all the analyses, including distances, classification and correlations, are based on the model representation with all the units in the corresponding layer as described above. For each model and each image, we computed the Euclidian distance between the model's representation and the mean point across all whole objects within the corresponding category. This distance-to-category corresponds to the y-axis in **Figure 3C-D**. We schematically illustrate the distance-to-category in **Figure 3B**, but we note that this schematic is not mathematically accurate because the t-SNE embeddings are not directly reflective of distances used in the calculations in **Figure 3C-D**.

Recurrent Neural Network Models

A recurrent neural network (RNN) was constructed by adding all-to-all recurrent connections to the top feature layer of AlexNet (**Figure 4A**). An RNN consists of a state vector that is updated according to the input at the current time

step and its value at the previous time step. Denoting \mathbf{h}_t as the state vector at time t and \mathbf{x}_t as the input into the network at time t , the general form of the RNN update equation is $\mathbf{h}_t = f(\mathbf{W}_h \mathbf{h}_{t-1}, \mathbf{x}_t)$ where f introduces a non-linearity as defined below. In our model, \mathbf{h}_t represents the fc7 feature vector at time t and \mathbf{x}_t represents the feature vector for the previous layer, fc6, multiplied by the transition weight matrix $\mathbf{W}_{6 \rightarrow 7}$. For simplicity, the first six layers of AlexNet were kept fixed to their original feed-forward versions.

We considered several different ways of choosing the weights \mathbf{W}_h . The first version involved a Hopfield network (45), RNN_h , as implemented in MATLAB's *newhop* function. Since this implementation is based on binary unit activity, we first converted the scalar activities in \mathbf{x} to $\{-1, +1\}$ by mapping those values greater than 0 to +1 and all other value to -1. The weights in RNN_h are symmetric ($W_{ij} = W_{ji}$) and

are dictated by the Hebbian learning rule $W_{ij} = \frac{1}{n_p} \sum_{p=1}^{n_p} x_i^p x_j^p$ where the sum goes over the n_p patterns of whole objects to be stored (in our case $n_p=325$) and x_i^p represents the activity of unit i in response to pattern p . This model does not have any free parameters that depend on the partial objects and the weights are uniquely specified by the activity of the feed-forward network in response to the whole objects. After specifying \mathbf{W}_h , the activity in RNN_h was updated according to $\mathbf{h}_0 = \mathbf{x}$ and $\mathbf{h}_t = \text{satlins}(\mathbf{W}_h \mathbf{h}_{t-1} + \mathbf{b})$ for $t > 0$ where *satlins* represents the saturating linear transfer function, $\text{satlins}(z) = \max(\min(1, z), -1)$ and \mathbf{b} introduces a constant bias term. The activity in RNN_h was simulated until convergence, defined as the first time point where there was no change in the sign of any of the features between two consecutive time points.

We also considered two different versions of RNN models that were trained to reconstruct the feature representations of the whole objects from the feature representations of the corresponding partial objects (**Figures S4-S5**). The state at time $t > 0$ was computed as the activation of the weighted sum of the previous state and the input from the previous layer: $\mathbf{h}_t = \text{ReLU}(\mathbf{W}_h \mathbf{h}_{t-1} + \mathbf{x})$ where

$\text{ReLU}(z) = \max(0, z)$. The loss function was the mean squared Euclidean distance between the features from the partial objects and the features from the whole objects. Specifically, the RNN was iterated for a fixed number of time steps ($t_{max} = 4$) after the initial feed-forward pass, keeping the input from fc6 constant. Thus, letting

$\mathbf{h}_{t_{max}}^p$ be the RNN state at the last time step for a given image pattern p and $\hat{\mathbf{h}}_{t_0}^p$ be the feed-forward feature vector of the corresponding whole image pattern, the loss function has the form

$$E = \frac{1}{T_p} \sum_{p=1}^{T_p} \left[\frac{1}{T_u} \sum_{j=1}^{T_u} (\mathbf{h}_{t_{max}}^p[j] - \hat{\mathbf{h}}_{t_0}^p[j])^2 \right]$$

where j goes over all the T_u units in fc7 and p goes over all the T_p images in the training set. The RNN was trained in a cross validated fashion (5 folds) using the same cross validation scheme as with the feed-forward models and using the algorithm RMSprop for optimization (50). In RNN₅, the weights of the RNN were trained with 260 objects for each fold. All of the partial objects from the psychophysics experiment for the given 260 objects, as well as one copy of the original 260 images, were used to train the RNN for the corresponding split. In the case where the input to the RNN was the original image itself, the network did not change its representation over the recurrent iterations. Given the high number of weights to be learned by the RNN as compared to the number of training examples, the RNNs overfit fairly quickly. Therefore, early stopping (10 epochs) was implemented as determined from the validation set, i.e., we used the weights at the time step where the validation error was minimal. To evaluate the extent of extrapolation across categories, we considered an additional version, RNN₁. In RNN₁, the recurring weights were trained using objects from only one category and the model was tested using objects from the remaining 4 categories. In all RNN versions, once \mathbf{W}_h was fixed, classification performance was assessed using a linear SVM, as with the feed-forward models. Specifically, the SVM boundaries were trained using the responses from the feed-forward model to the whole objects and performance was evaluated using the representation at different time steps of recurrent computation.

We ran an additional simulation with the RNN models to evaluate the effects of backward masking (**Figure 4F, S5**). For this purpose, we simulated the response of the feed-forward AlexNet model to the same masks used for the psychophysical experiments to determine the fc6 features for each mask image. Next, we used this mask as the fixed input \mathbf{x}_t into the recurrent network, beginning at different time points after the initial image input.

Code availability. All the code will be made available through the Kreiman lab web site and also through the Kreiman lab GitHub repository.

Funding

This work was supported by a fellowship from the FITweltweit programme of the German Academic Exchange Service (DAAD) (MS), NSF STC award CCF-123121 (GK) and NIH award R01EY026025 (GK).

Acknowledgments

We thank Carlos Ponce, Alan Yuille, Siamak Sorooshyari and Guy Ben-Yosef for useful discussions and comments.

Data availability statement

All relevant data and code (including image databases, behavioral measurements, physiological measurements and computational algorithms) will be made available upon publication through the lab's publicly accessible GitHub.

Author contributions

Conceptualization: HT, BL, MS, DC, GK

Physiology experiment design: HT, GK

Physiological data collection and analyses: HT

Psychophysics experiment design: HT, BL, GK

Psychophysics data collection: HT, BL, MS, AP, JO, WH

Computational models: HT, BL, MS, DC, GK

Resources: DC, GK

Manuscript writing: HT, BL, MS, GK

References

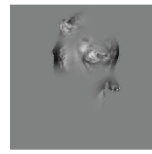
1. Logothetis NK & Sheinberg DL (1996) Visual object recognition. *Annual Review of Neuroscience* 19:577-621.
2. Tanaka K (1996) Inferotemporal cortex and object vision. *Annual Review of Neuroscience* 19:109-139.
3. DiCarlo JJ & Cox DD (2007) Untangling invariant object recognition. *Trends Cogn Sci* 11(8):333-341.
4. Riesenhuber M & Poggio T (1999) Hierarchical models of object recognition in cortex. *Nature Neuroscience* 2(11):1019-1025.
5. Serre T, *et al.* (2007) A quantitative theory of immediate visual recognition. *Progress In Brain Research* 165C:33-56.
6. Rolls E (1991) Neural organization of higher visual functions. *Current opinion in neurobiology* 1:274-278.
7. Connor CE, Brincat SL, & Pasupathy A (2007) Transformation of shape information in the ventral pathway. *Current opinion in neurobiology* 17(2):140-147.
8. Krizhevsky A, Sutskever I, & Hinton G (2012) ImageNet Classification with Deep Convolutional Neural Networks. in *NIPS* (Montreal).
9. Yamins DL, *et al.* (2014) Performance-optimized hierarchical models predict neural responses in higher visual cortex. *Proceedings of the National Academy of Sciences of the United States of America* 111(23):8619-8624.
10. Kellman PJ, Guttman S, & Wickens T (2001) Geometric and neural models of object perception. *From framents to objects: Segmentation and grouping in vision*, eds Shipley TF & Kellman PJ (Elsevier Science Publishers, Oxford, UK).
11. Murray RF, Sekuler AB, & Bennett PJ (2001) Time course of amodal completion revealed by a shape discrimination task. *Psychon Bull Rev* 8(4):713-720.
12. Kosai Y, El-Shamayleh Y, Fyall AM, & Pasupathy A (2014) The role of visual area V4 in the discrimination of partially occluded shapes. *Journal of Neuroscience* 34(25):8570-8584.
13. Nakayama K, He Z, & Shimojo S (1995) Visual surface representation: a critical link between lower-level and higher-level vision. *Visual cognition*, eds Kosslyn S & Osherson D (The MIT press, Cambridge), Vol 2.
14. Tang H, *et al.* (2014) Spatiotemporal dynamics underlying object completion in human ventral visual cortex. *Neuron* 83:736-748.
15. Johnson JS & Olshausen BA (2005) The recognition of partially visible natural objects in the presence and absence of their occluders. *Vision research* 45(25-26):3262-3276.
16. Lee TS (2003) Computations in the early visual cortex. *J Physiol Paris* 97(2-3):121-139.

17. Brown JM & Koch C (2000) Influences of occlusion, color, and luminance on the perception of fragmented pictures. *Percept Mot Skills* 90(3 Pt 1):1033-1044.
18. Gilbert CD & Li W (2013) Top-down influences on visual processing. *Nat Rev Neurosci* 14(5):350-363.
19. Angelucci A & Bressloff PC (2006) Contribution of feedforward, lateral and feedback connections to the classical receptive field center and extra-classical receptive field surround of primate V1 neurons. *Prog Brain Res* 154:93-120.
20. Bregman AL (1981) *Asking the "what for" question in auditory perception* (Erlbaum, Hillsdale, NJ) p 19.
21. Kirchner H & Thorpe SJ (2006) Ultra-rapid object detection with saccadic eye movements: visual processing speed revisited. *Vision research* 46(11):1762-1776.
22. Potter M & Levy E (1969) Recognition memory for a rapid sequence of pictures. *Journal of experimental psychology* 81(1):10-15.
23. Keysers C, Xiao DK, Foldiak P, & Perret DI (2001) The speed of sight. *Journal of Cognitive Neuroscience* 13(1):90-101.
24. Hung CP, Kreiman G, Poggio T, & DiCarlo JJ (2005) Fast Read-out of Object Identity from Macaque Inferior Temporal Cortex. *Science* 310:863-866.
25. Liu H, Agam Y, Madsen JR, & Kreiman G (2009) Timing, timing, timing: Fast decoding of object information from intracranial field potentials in human visual cortex. *Neuron* 62(2):281-290.
26. Tovee M & Rolls E (1995) Information encoding in short firing rate epochs by single neurons in the primate temporal visual cortex. *Visual Cognition* 2(1):35-58.
27. Pinto N, Doukhan D, DiCarlo JJ, & Cox DD (2009) A high-throughput screening approach to discovering good forms of biologically inspired visual representation. *PLoS Comput Biol* 5(11):e1000579.
28. Wallis G & Rolls ET (1997) Invariant face and object recognition in the visual system. *PROGRESS IN NEUROBIOLOGY* 51(2):167-194.
29. Serre T, Oliva A, & Poggio T (2007) Feedforward theories of visual cortex account for human performance in rapid categorization. *PNAS* 104(15):6424-6429.
30. Breitmeyer B & Ogmen H (2006) *Visual Masking: Time Slices through Conscious and Unconscious Vision* (Oxford University Press, New York).
31. Bridgeman B (1980) Temporal response characteristics of cells in monkey striate cortex measured with metacontrast masking and brightness discrimination. *Brain Res* 196(2):347-364.
32. Macknik SL & Livingstone MS (1998) Neuronal correlates of visibility and invisibility in the primate visual system. *Nature neuroscience* 1(2):144-149.
33. Lamme VA, Zipser K, & Spekreijse H (2002) Masking interrupts figure-ground signals in V1. *J Cogn Neurosci* 14(7):1044-1053.
34. Kovacs G, Vogels R, & Orban GA (1995) Cortical correlate of pattern backward masking. *Proceedings of the National Academy of Sciences* 92(12):5587-5591.

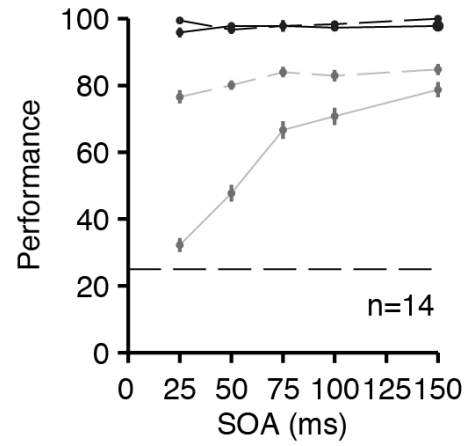
35. Rolls ET, Tovee MJ, & Panzeri S (1999) The neurophysiology of backward visual masking: information analysis. *Journal of Cognitive Neuroscience* 11(3):300-311.
36. Keysers C & Perrett DI (2002) Visual masking and RSVP reveal neural competition. *Trends Cogn Sci* 6(3):120-125.
37. Enns JT & Di Lollo V (2000) What's new in visual masking? *Trends Cogn Sci* 4(9):345-352.
38. Thompson KG & Schall JD (1999) The detection of visual signals by macaque frontal eye field during masking. *Nature neuroscience* 2(3):283-288.
39. Fukushima K (1980) Neocognitron: a self organizing neural network model for a mechanism of pattern recognition unaffected by shift in position. *Biological Cybernetics* 36(4):193-202.
40. Simonyan K & Zisserman A (2014) Very deep convolutional networks for large-scale image recognition. *arXiv* 1409.1556.
41. Rumelhart DE, Hinton G, & Williams RJ (1986) Learning representations by back-propagating errors. *Nature* 323:533-536.
42. Pepik B, Benenson R, Ritschel T, & Schiele B (2015) What is holding back convnets for detection? 1508.
43. Wyatte D, Curran T, & O'Reilly R (2012) The limits of feedforward vision: recurrent processing promotes robust object recognition when objects are degraded. *J Cogn Neurosci* 24(11):2248-2261.
44. van der Maaten L & Hinton G (2008) Visualizing High-Dimensional Data Using t-SNE. *J. Machine Learning Res.* 9:2579-2605.
45. Hopfield JJ (1982) Neural networks and physical systems with emergent collective computational abilities. *PNAS* 79:2554-2558.
46. Stettler D, Das A, Bennett J, & Gilbert C (2002) Lateral Connectivity and Contextual Interactions in Macaque Primary Visual Cortex. *Neuron* 36:739-750.
47. Nassi J, Lomber S, & Born R (2013) Corticocortical Feedback Contributes to Surround Suppression in V1 of the Alert Primate. *Journal of Neuroscience* 33(19):8504.
48. Gosselin F & Schyns PG (2001) Bubbles: a technique to reveal the use of information in recognition tasks. *Vision research* 41(17):2261-2271.
49. Yangqing J, *et al.* (2014) Caffe: Convolutional Architecture for Fast Feature Embedding. *arXiv*:1408.5093.
50. Tieleman T & Hinton G (2012) Lecture 6.5-rmsprop: Divide the gradient by a running average of its recent magnitude. . 4.

Supplementary Figure 1

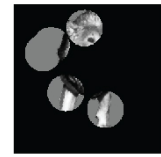
A



Partial



B



Occluded

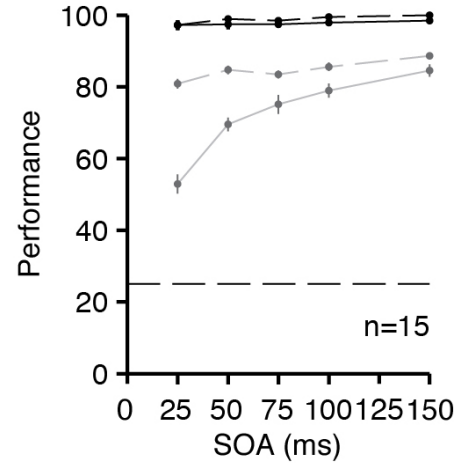


Figure S1: Robust performance with occluded stimuli

We measured categorization performance with masking (solid lines) or without masking (dashed lines) for (A) partial and (B) occluded stimuli on a set of 16 exemplars belonging to 4 categories (chance = 25%, dashed lines). There was no overlap between the 14 subjects that participated in (A) and the 15 subjects that participated in (B). The effect of backward masking was consistent across both types of stimuli. The black lines indicate whole objects and the gray lines indicate the partial and occluded objects. Error bars denote s.e.m.

Supplementary Figure 2

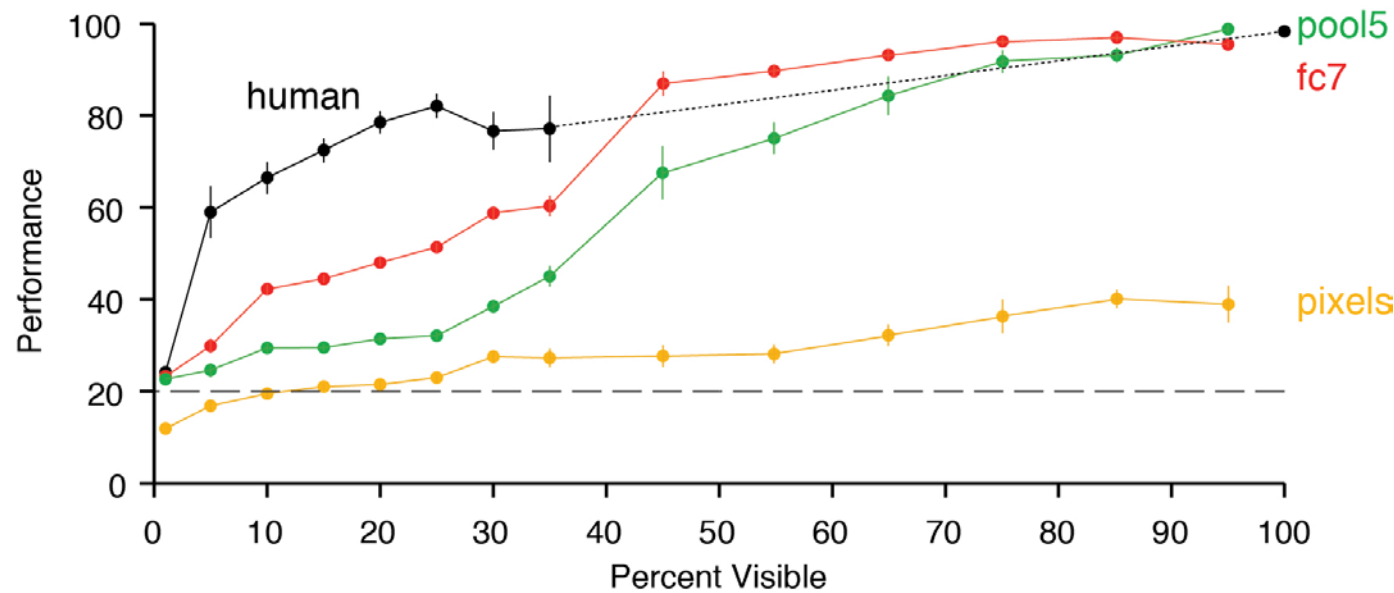


Figure S2: Bottom-up models can recognize minimally occluded images

Extension to **Fig. 3A** showing that bottom-up models successfully recognize objects when more information is available (**Fig. 3A** showed visibility values up to 35% whereas this figure extends visibility up to 95%). The format and conventions are the same as those in **Fig. 3A**. The black dotted line shows interpolated human performance between the psychophysics experimental values measured at 35% and 100% visibility levels.

Supplementary Figure 3

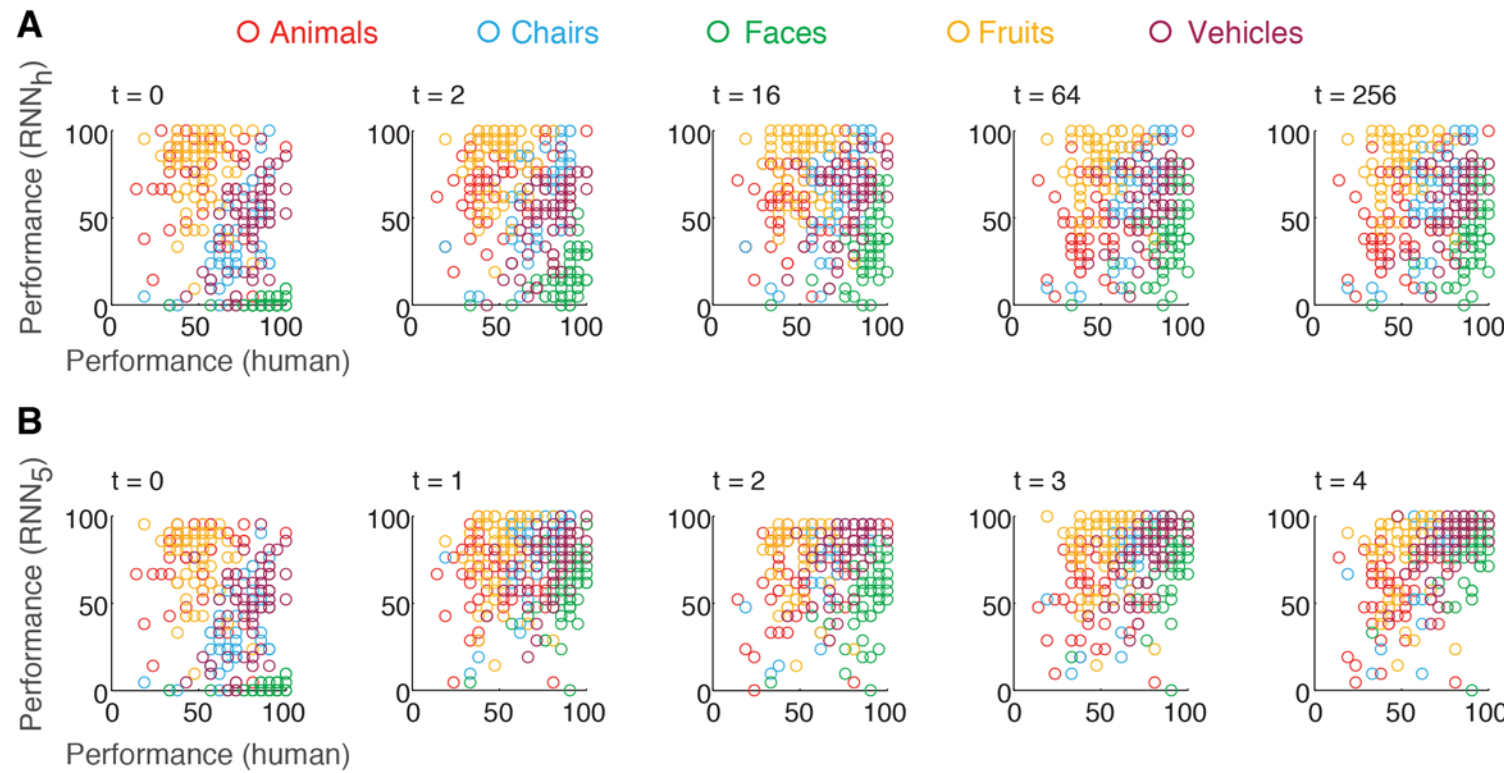


Figure S3: Correlation between RNN models and human performance for individual objects as a function of time

At each time step in the recurrent neural network model (**A**: RNN_h, **B**: RNN₅), the scatter plots show the relationship between the model's performance on individual partial exemplar objects and human performance. Each dot is an individual exemplar object. In **Fig. 4F** we report the average correlation coefficient across all categories.

Supplementary Figure 4

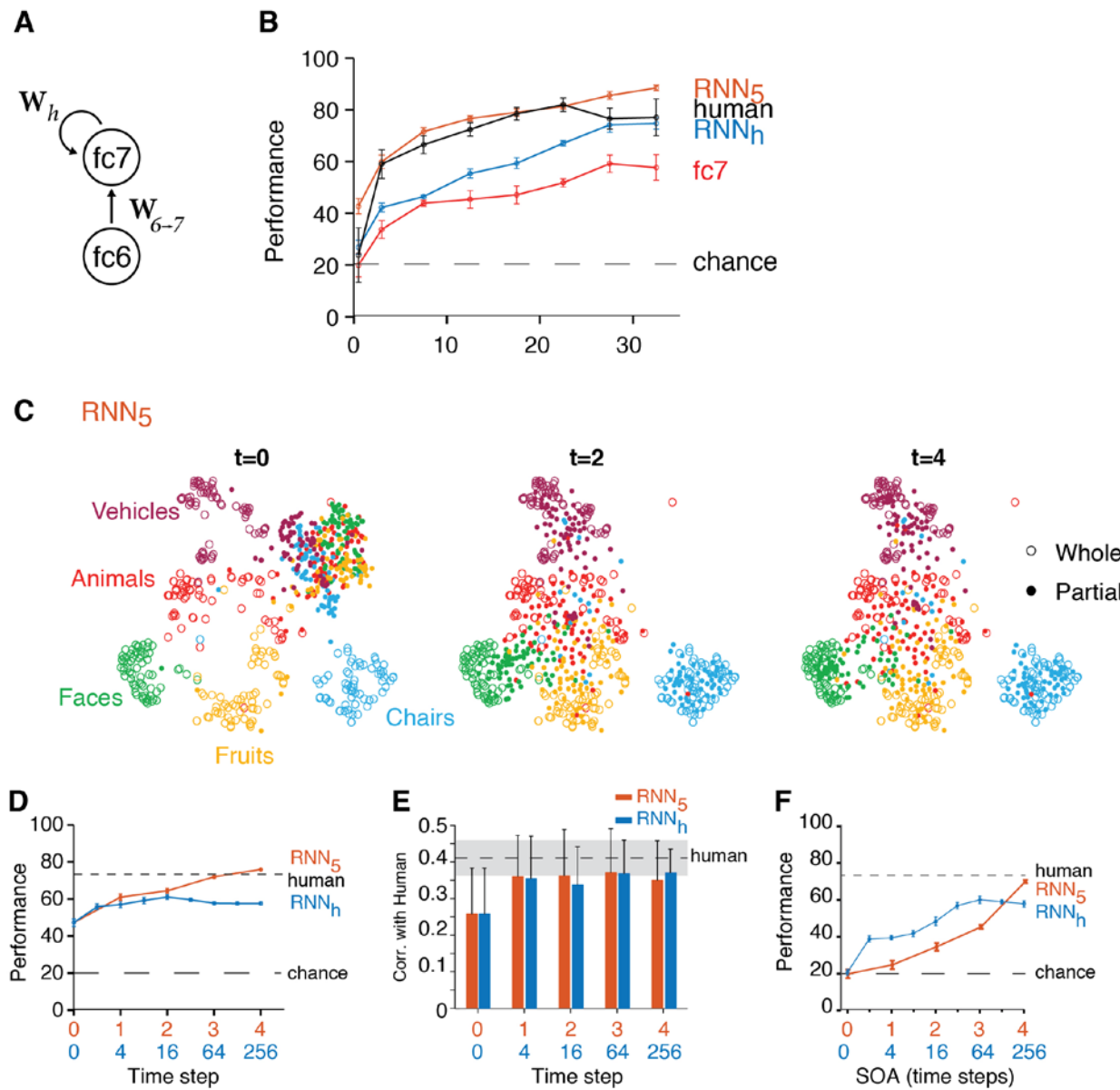


Figure S4: Extension to Figure 4 in the main text showing results for RNN₅. The format and conventions for this figure follow those in **Fig. 4**. The orange symbols here describe the results for the RNN₅ model. We reproduce here the results from **Fig. 4** for comparison purposes.

Supplementary Figure 5

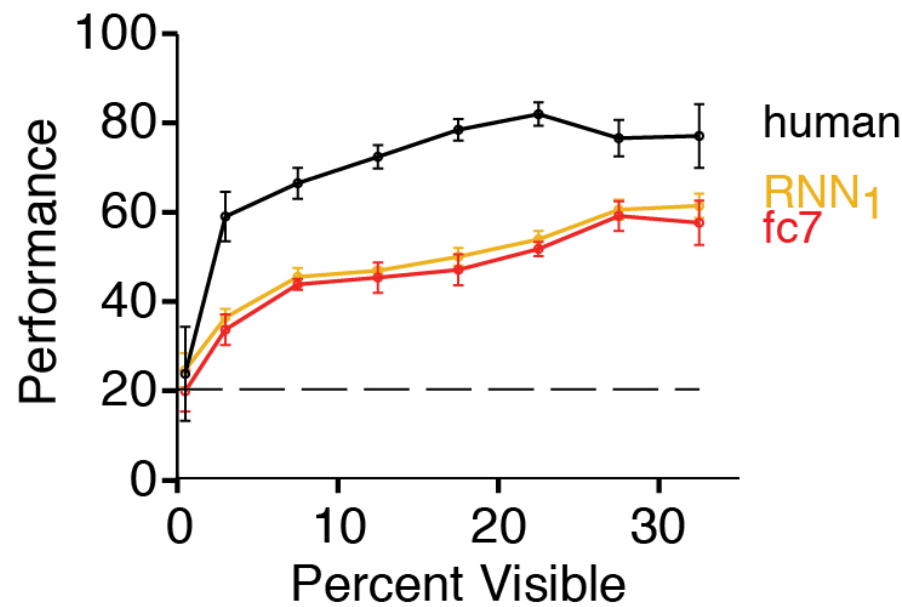


Figure S4: Performance of the RNN₁ model

Using the same format and conventions as in **Fig. 4B**, we show performance as a function of object visibility for the RNN₁ model. The performance of the fc7 model and human performance are copied from **Fig. 4B** for comparison purposes.

Supplementary Figure 6

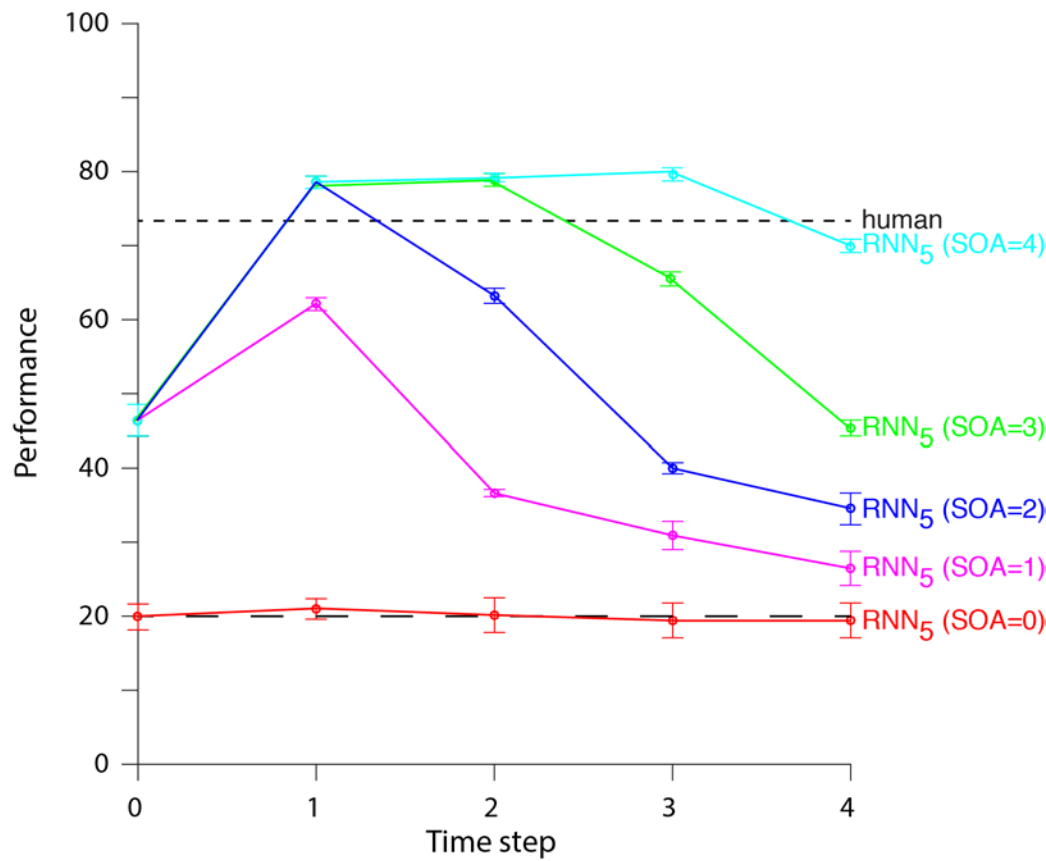


Figure S6: Performance of RNN₅ during backward masking

Expanding on the presentation in **Fig. 4F**, here we show the performance of the RNN₅ model at different time steps upon introducing a backward mask at SOA values ranging from time step 0 (red) through time step 5 (cyan). The format and conventions are the same as in **Fig. 4F**.